

Magnetically-separable $\text{Fe}_3\text{O}_4@\text{SiO}_2@\text{SO}_4\text{-ZrO}_2$ core-shell nanoparticle catalysts for propanoic acid esterification

Zhijun Tai^a, Mark A. Isaacs^a, Lee J. Durndell^a, Christopher M.A. Parlett^a, Adam F. Lee^b, Karen Wilson^{b,*}

^a European Bioenergy Research Institute, Aston University, Birmingham, B4 7ET, UK

^b School of Science, RMIT University, Melbourne, VIC 3001, Australia



ARTICLE INFO

Keywords:

Magnetic nanoparticles
Sulfated zirconia
Solid acid
Core-shell
Esterification

ABSTRACT

Monodispersed, sulfated zirconia encapsulated magnetite nanoparticles were synthesized as magnetically-separable solid acid catalysts. Catalyst nanoparticles are prepared via coating preformed 80 nm Fe_2O_3 particles with a 15 nm SiO_2 protective coating prior to growth of a uniform 28 nm ZrO_2 shell. The thickness of the ZrO_2 shell in resulting $\text{Fe}_3\text{O}_4@\text{SiO}_2@\text{ZrO}_2$ nanoparticles was controlled by adjusting the zirconium butoxide to Lutensol AO5 ratio, with 1:10 found as the optimal ratio to produce monodispersed ZrO_2 coated nano-spheres. Sulfation using an ammonium sulfate precursor is less corrosive towards the core-shell structure of $\text{Fe}_3\text{O}_4@\text{SiO}_2@\text{ZrO}_2$ nanoparticles leading to superior sulfated materials compared to those obtained using H_2SO_4 . Resulting $\text{Fe}_3\text{O}_4@\text{SiO}_2@\text{SO}_4\text{-ZrO}_2$ solid acid catalysts exhibit high activity for propanoic acid esterification with methanol, far exceeding that of conventional sulfated zirconia nanoparticles, while being amenable to facile magnetic separation.

1. Introduction

Functionalized nano- and microparticles possessing core-shell structures have attracted great interest in recent decades for potential applications in drug delivery, magnetic resonance imaging, bioassays, and catalysis [1–6]. Various approaches have been exploited to synthesize core-shell nanospheres, including the “Stöber” approach [7], microemulsions/reverse-micelle [8,9], and aerosol pyrolysis [10], which enable the fabrication of monodispersed nanomaterials with complex structures including onion-like architectures. In regard of catalysis, magnetic nanoparticles and core-shell variants are particularly attractive since they offer high surface areas, and facile catalyst separation/recycling and product recovery, and hence are ideally suited to liquid phase transformations such as cellulose hydrolysis [11], fructose dehydration [12], aldol condensation of 5-hydroxymethylfurfural (5-HMF) with ethanol [13], oxidation of 5-HMF to 2,5-diformylfuran [14], carboxylic acid esterification, [15] and biodiesel production [16,17]. Magnetically separable solid acid nanoparticles typically comprise organic functions and therefore suffer poor thermal stability; [18] more robust inorganic analogues are therefore desirable.

Zirconia is widely used in materials science, notably as a semiconductor [19], thermal barrier coating [20], component of oxygen

sensors [21], and a heterogeneous solid acid catalyst wherein its amphoteric Lewis and Brønsted acid character facilitates cascade reactions [22]. Sulfated zirconia (SZ) is generally considered a superacid catalyst that exhibits predominantly Brønsted character and high activity for diverse liquid phase reactions [23–25], however, conventional synthetic routes to SZ typically result in a low surface area and porosity. Recovery and recycling of such metal oxide heterogeneous catalysts is also problematic, and hence the development of magnetically-separable and highly dispersed SZ nanostructures is especially desirable. There are only a few reports on the synthesis of magnetic zirconia nanoparticles [26–30], and these do not produce well-defined or monodispersed core-shell nanoparticles.

Yin et al. recently developed a new, room temperature synthesis of monodispersed zirconia encapsulated polystyrene (PS) nanospheres, $\text{PS}@ZrO_2$ employing the PS nanospheres as a hard template [31]. Hollow ZrO_2 nanospheres were subsequently fabricated by calcination to remove the PS template. Schüth et al. [32] adopted a different approach to create hollow ZrO_2 nanospheres utilizing silica nanospheres as the hard template in conjunction with the nonionic amphiphilic surfactant Lutensol AO5; the silica core was subsequently etched by dilute NaOH resulting in high surface area ($300\text{ m}^2\text{ g}^{-1}$) hollow zirconia spheres. A modified protocol allowed the preparation of yolk-shell $\text{Au}@ZrO_2$ nanospheres in which the hollow ZrO_2 shell protected

* Corresponding author.

E-mail address: karen.wilson2@rmit.edu.au (K. Wilson).

small Au nanoparticles confined within the internal void against thermal sintering [32]. To our knowledge sulfated analogues of such monodispersed zirconia nanospheres (or core-shell variants) have not been synthesized, while the only report of magnetic sulfated zirconia nanoparticles produced inhomogeneous materials lacking a well-defined magnetic core-SZ shell structure.

Herein, we report the first synthesis and catalytic application of monodispersed magnetic SZ nanoparticles possessing an onion skin structure comprising a magnetite core, encapsulated by a protecting, dense silica shell, which is in turn enveloped by a conformal SZ shell of tunable thickness between 6 and 28 nm ($\text{Fe}_3\text{O}_4@\text{SiO}_2@\text{SZ}$). These magnetic SZ nanoparticles were subsequently evaluated for propanoic acid esterification, a prototypical solid acid catalyzed reaction employed to upgrade biomass derived pyrolysis-oil [33–35] which are intrinsically unstable and corrosive due to C_2 - C_3 acid components [36].

2. Experimental

2.1. Catalyst synthesis

2.1.1. Synthesis of silica encapsulated iron oxide nanoparticles ($\text{Fe}_2\text{O}_3@\text{SiO}_2$)

Silica encapsulated iron oxide nanoparticles were synthesized using a modified version of the method of Zhao et al. [37] Uniform hematite (Fe_2O_3) particles were first obtained by aging a 0.02 M aqueous FeCl_3 solution at 100 °C for 48 h, with the resulting Fe_2O_3 nanoparticles isolated by centrifugation, then washed three times with 2-propanol. 50 mg of the resulting Fe_2O_3 nanoparticles were then added to a mixture of 200 mL 2-propanol, 40 mL H_2O , and 5 mL of 35 vol% aqueous ammonia while stirring. To this nanoparticle suspension, 0.15 mL of tetraethyl orthosilicate was added dropwise under vigorous stirring and the resulting mixture aged at room temperature overnight to yield silica encapsulated iron oxide nanoparticles upon centrifugation.

2.1.2. Preparation of magnetic zirconia encapsulated Fe_3O_4 nanoparticles ($\text{Fe}_3\text{O}_4@\text{SiO}_2@\text{ZrO}_2$)

The as-synthesized $\text{Fe}_2\text{O}_3@\text{SiO}_2$ nanoparticles were added to 100 mL ethanol containing the desired volume (0.25 mL–1.5 mL) of Lutensol AO5 solution (0.43 g Lutensol AO5 dissolved in 11 g of H_2O). The mixture was stirred for 1 h at room temperature, and then the desired amount (0.05 mL–0.9 mL) of zirconium (IV) butoxide was added quickly. The solution was kept at room temperature and stirred vigorously overnight. The resulting nanoparticles were centrifuged, re-dispersed in water, and then aged at room temperature for 3 days. Subsequently the nanoparticles were centrifuged and calcined at 900 °C (ramp rate 2 °C/min) for 2 h to yield zirconia encapsulated $\text{Fe}_2\text{O}_3@\text{SiO}_2@\text{ZrO}_2$ nanoparticles. These were finally reduced under flowing H_2 at 450 °C (ramp rate 2 °C/min) for 2 h to convert the hematite core into magnetite (Fe_3O_4).

2.1.3. Preparation of magnetic sulfated zirconia (nanoparticles) $\text{Fe}_3\text{O}_4@\text{SiO}_2@\text{SO}_4\text{-ZrO}_2$

$\text{Fe}_3\text{O}_4@\text{SiO}_2@\text{ZrO}_2$ prepared with a zirconium butoxide:Lutensol AO5 vol ratio of 0.45 mL:0.25 mL were selected as the parent. Sulfation was performed through either wet impregnation with H_2SO_4 or incipient-wetness impregnation by $(\text{NH}_4)_2\text{SO}_4$. For wet impregnation, 0.4 g of $\text{Fe}_3\text{O}_4@\text{SiO}_2@\text{ZrO}_2$ nanoparticles were added to 30 mL aqueous H_2SO_4 (0.05–0.20 M) with stirring at room temperature for 5 h. The resulting sulfated nanoparticles were magnetically separated, dried overnight in an oven, and then annealed under flowing N_2 at 550 °C (ramp rate 2 °C/min) for 3 h. Incipient-wetness impregnation was performed by mixing 0.3 g of $\text{Fe}_3\text{O}_4@\text{SiO}_2@\text{ZrO}_2$ nanoparticles with 1 mL of deionized water containing 0.3 g of $(\text{NH}_4)_2\text{SO}_4$, followed by drying overnight in an oven, and then annealed under flowing N_2 at 550 °C (ramp rate 2 °C/min) for 3 h.

Prior to use, both types of sulfated $\text{Fe}_3\text{O}_4@\text{SiO}_2@\text{ZrO}_2$ nanoparticles

were stirred with methanol at 60 °C for 4 h to remove physisorbed sulfate. Magnetic sulfated zirconia particles prepared with H_2SO_4 , are designated xMSZ where $x = [\text{H}_2\text{SO}_4]$, those prepared with ammonium sulfate are designated NH_4MSZ .

For comparison, a pure sulfated zirconia (SZ) was prepared by conventional wet impregnation with H_2SO_4 [22]. 2.5 g of $\text{Zr}(\text{OH})_4$ (MEL Chemicals-XZO 880/01) was added to 25 mL aqueous H_2SO_4 (0.2 M). The resulting slurry was stirred for 5 h at room temperature, filtered, and dried at 80 °C overnight, prior to calcination in air at 550 °C (ramp rate 2 °C/min) for 3 h.

2.2. Catalyst characterization

Textural and structural properties of parent core-shell nanoparticles and the corresponding sulfated nanoparticles were measured by a combination of N_2 porosimetry and transmission electron microscopy (TEM). Nitrogen physisorption was undertaken on a Quantachrome Nova 1200 instrument, with samples degassed at 120 °C for 6 h prior to recording N_2 adsorption/desorption isotherms. Brunauer–Emmett–Teller (BET) surface areas were calculated over the relative pressure range 0.01–0.2 (P/P_0), while pore size distributions were calculated using the Barrett–Joyner–Halenda (BJH) method applied to the desorption branch of the isotherm. Transmission electron microscopy (TEM) images were recorded on an aberration corrected JEOL 2100-F electronic microscope operating at 200 kV; equipped with a Gatan Orius SC600A CCD camera. Samples were prepared by dispersion in ethanol and drop-casting onto a copper grid coated with a holey carbon support film (Agar Scientific Ltd). Images were analysed using Image J 1.41 software.

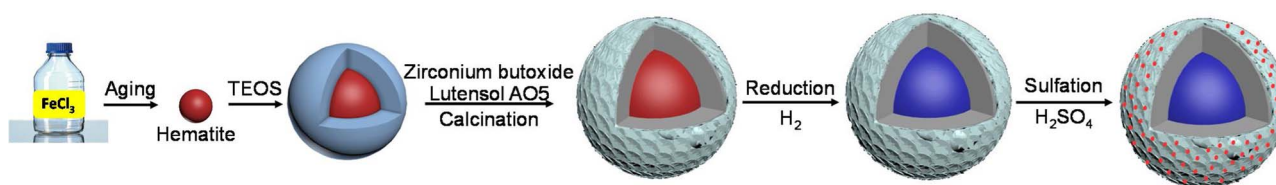
Bulk sulfur elemental analysis was performed on a FLASH 2000 CHNS/O organic elemental analyzer. XPS was performed on a Kratos Axis HSi X-ray photoelectron spectrometer fitted with a charge neutralizer and magnetic focusing lens employing Al K α monochromated radiation (1486.7 eV); spectral fitting was performed using Casa XPS version 2.3.15, with spectra energy-corrected to the C 1s peak of adventitious carbon at 284.6 eV.

Acid site loadings were quantified by propylamine decomposition via the Hoffman reaction, using a thermo-gravimetric mass spectrometry analysis (TGA-MS) method [38]. Prior to thermogravimetric analysis, samples were impregnated with propylamine and then dried in the vacuum oven at 40 °C overnight. TGA was performed on a Mettler Toledo, TGA/DSC2 Star system with a heating rate of 10 °C/min from 40 to 800 °C with flowing N_2 (30 mL min⁻¹). In parallel, evolved gas analysis was performed with Pfeiffer ThermoStar mass spectrometer, connected to the outlet of the TGA apparatus. Mass channels were recorded for m/z values of 17 (NH_3), 41 (propene) and 59 (propylamine), with the evolution of reactively propene a product from propylamine decomposition over acid sites.

Brønsted/Lewis acid character was determined by pyridine DRIFT, carried out by impregnation of diluted samples (10 wt% in KBr) with neat pyridine. Excess physisorbed pyridine was removed in a vacuum oven at 30 °C overnight prior to sample loading in the environmental cell. DRIFT spectra of the pyridine-saturated samples were recorded at room temperature under vacuum using a Nicolet Avatar 370 MCT with Smart Collector accessory, mid/near infrared source and a mercury cadmium telluride (MCT-A) photon detector at –196 °C.

2.3. Propanoic acid esterification

Esterification was carried out on a Radleys Starfish carousel at 60 °C using a stirred batch reactor at atmospheric pressure. Reactions were conducted with 10 mmol of propanoic acid in 12.5 mL of methanol (molar ratio $n_{\text{MeOH}}/n_{\text{PA}} = 30$), 50 mg of catalyst and 0.59 mL of dihexylether as an internal standard. Samples were withdrawn periodically, separated with a strong magnet and diluted with methanol prior to analysis on a gas chromatograph (Varian 450-GC, Phenomenex ZB-50 15 m × 0.53 mm × 1.0 μm capillary column, FID detector).



Scheme 1. Stepwise synthesis of magnetically-separable $\text{Fe}_3\text{O}_4@SiO_2@SO_4\text{-ZrO}_2$ core-shell nanoparticle catalysts.

3. Results and discussion

The multistep synthesis of magnetic SZ core-shell nanoparticles illustrated in Scheme 1 was as follows (details provided in the Supporting Information). Monodispersed, 80 nm hematite (Fe_2O_3) nanoparticles were first prepared following the hydrothermal route of Matijević and Scheiner [39]. A dense silica layer was subsequently deposited by a classical Stöber method, to protect the iron core from corrosion and leaching during catalytic application, with the resulting $\text{Fe}_2\text{O}_3@SiO_2$ nanoparticles exhibiting a sharp core-shell interface and uniform 15 nm silica shells (Fig. S1 in the Supporting Information). The silica shell thickness could be adjusted by varying the concentration of TEOS (tetraethyl orthosilicate) precursor.

A zirconia shell was then grown around the $\text{Fe}_2\text{O}_3@SiO_2$ nanoparticles following the protocol of Schüth and co-workers, in which zirconium (IV) butoxide was hydrolysed in dry ethanol over the particles (whose surfaces were pre-modified by the adsorption of Lutensol AO5 surfactant), prior to aging in water at room temperature for three days and 900 °C calcination to obtain $\text{Fe}_2\text{O}_3@SiO_2@ZrO_2$ onion-skin structures (Fig. 1a and b). The ZrO_2 shell was uniform and approximately 28 nm thick, however the shell thickness and morphology could be adjusted by varying the ratio of zirconium (IV) butoxide to Lutensol AO5. $\text{Fe}_2\text{O}_3@SiO_2@ZrO_2$ nanoparticles agglomerated for high Zr:surfactant ratios (3.6:1 by volume), as seen in Fig. 1c, possibly due to poor conformal zirconia growth. Decreasing the Zr:surfactant ratio reduced the zirconia shell thickness, improved its uniformity, and suppressed particle agglomeration (Fig. 1d–e). The reduction in shell thickness to only 6.5 nm for the optimal 1:10 Zr:surfactant volumetric ratio could be reversed without any negative impact on particle morphology by simply increasing the concentrations of both zirconium (IV) butoxide and Lutensol AO5, while maintaining this optimal ratio, to achieve an outer shell of 10.6 nm (Fig. 1e). $\text{Fe}_2\text{O}_3@SiO_2@ZrO_2$ nanoparticles exhibited high surface areas spanning 63–111 $\text{m}^2\cdot\text{g}^{-1}$ (Table S1 in the Supporting Information). $\text{Fe}_2\text{O}_3@SiO_2@ZrO_2$ nanoparticles were then subject to a 450 °C treatment under H_2 to reduce the hematite core to magnetite (Fe_3O_4) [37] and hence facilitate their magnetic separation (Fig. 1f). The resulting magnetic core-shell nanoparticles exhibited significant mesoporosity (BJH analysis revealed ~2.9 nm diameter mesopores, Fig. S2 in Supporting Information). Following reduction, the zirconia shell comprised solely tetragonal ZrO_2 crystallites of ~6.4 nm diameter (Fig. S3 and Table S2 in the Supporting Information).

The final step involved sulfation of the zirconia shell via wet impregnation with dilute H_2SO_4 [24] (xMSZ, where $x = [H_2SO_4]$) or

incipient-wetness impregnation with aqueous $(NH_4)_2SO_4$, [40] (NH_4MSZ), followed by annealing at 550 °C under N_2 . For this, $\text{Fe}_3\text{O}_4@SiO_2@ZrO_2$ nanoparticles were prepared using a 2:1 ratio of zirconium butoxide:Lutensol AO5 in order to provide the optimum balance between zirconia film thickness, uniformity and surface area. Sulfation by H_2SO_4 had negligible effect on the shell crystallinity, with zirconia remaining in tetragonal form as 5–6 nm particles (Fig. S3 and Table S2 in the Supporting Information), but increased the surface area and pore volume relative to the unsulfated parent, possibly reflecting corrosion of the zirconia and underlying silica shells. The latter hypothesis is supported by TEM, which evidenced numerous hollow nanoparticles following sulfation by H_2SO_4 (Fig. S4 in the Supporting Information) consistent with leaching of iron from the Fe_3O_4 cores. In contrast, the NH_4MSZ material exhibited a significant decrease in surface area relative to the parent $\text{Fe}_2\text{O}_3@SiO_2@ZrO_2$, but retained magnetic Fe_3O_4 cores (Fig. S5 in the Supporting Information), presumably due to the weaker acidity of the ammonium precursor. Zr 3d XP spectra (Fig. 2) confirmed that the local zirconium chemical environment in the sulfated shell of the magnetic nanoparticles was identical to that observed within nanocrystalline sulfated zirconia, with a $3d_{5/2}$ binding energy of 182.5 eV [25,41,42]

The sulfur content of all sulphated core-shell nanoparticles was subsequently quantified by bulk and surface elemental analysis (Table 1), and for the H_2SO_4 impregnated materials was directly proportional to the sulfate concentration, with bulk values increasing from 0.21 → 0.47 wt%.

In contrast, incipient-wetness impregnation with a similar number of moles of $(NH_4)_2SO_4$ (2 mmoles per 0.3 g of sample) resulted in a S loading of 7.3 wt%. The trends in sulfur content were mirrored by corresponding acid site loadings determined by propylamine TPD (Table 1), [38] increasing from modest values of 0.25 → 0.4 $\text{mmol}(H^+)g^{-1}$ for the H_2SO_4 impregnated MSZs, whereas the NH_4MSZ material possessed 2.75 $\text{mmol}(H^+)g^{-1}$ far exceeding that observed for a pure SZ reference. Acid loadings determined by propylamine temperature-programmed decomposition are extremely surface sensitive, and only titrate sulfur in the outermost surface of the magnetic nanoparticles. In contrast, S 2p XP spectra probe almost all of the sulfur present in the top 3 nm of the sulfated zirconia shell, due to the long inelastic mean free path of ~1300 eV kinetic energy photoelectrons [43]. Table 1 shows that increasing the concentration of sulfuric acid used to impregnate the zirconia encapsulated magnetic nanoparticles resulted in greater penetration of sulfate ions throughout the zirconia matrix (detectable by XPS), but had little impact on the sulfate density in the terminating layer. Switching to an ammonium sulfate precursor

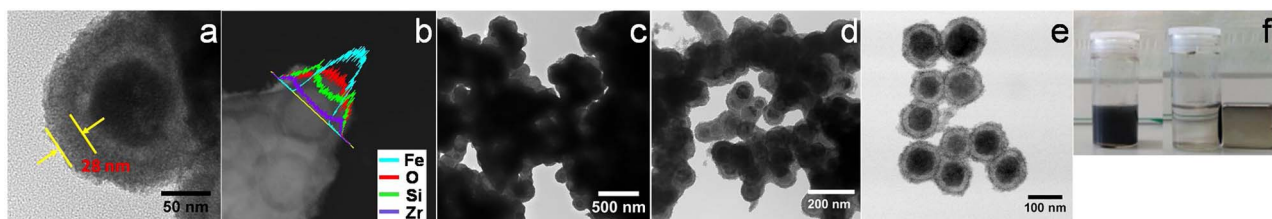


Fig. 1. a) TEM image of $\text{Fe}_2\text{O}_3@SiO_2@ZrO_2$ prepared with a zirconium butoxide (mL):Lutensol AO5 (mL) ratio of 0.90:0.25, and b) corresponding elemental line profile highlighting layered structure. Impact of changing zirconium butoxide (mL):Lutensol AO5 (mL) ratio on morphology of the core shell structure: c) 0.9:0.25, d) 0.3:0.25, and e) 0.15:1.5. f) magnetic separation of NH_4MSZ post-reaction.

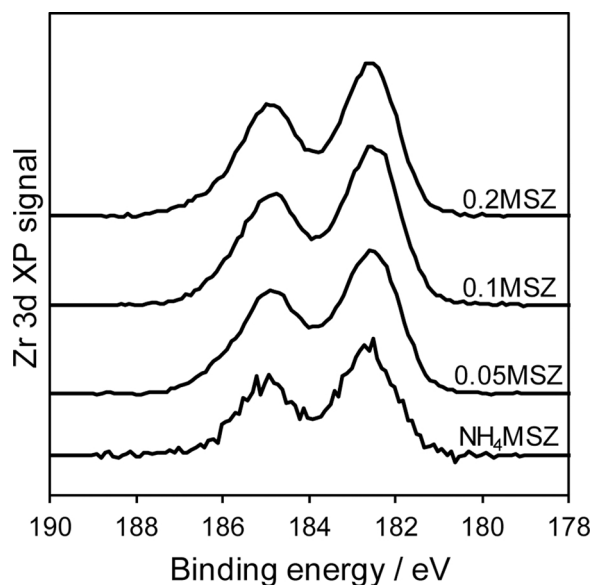


Fig. 2. Zr 3d XP spectra of magnetic sulfated $\text{Fe}_3\text{O}_4@\text{SiO}_2@\text{ZrO}_2$ nanoparticles.

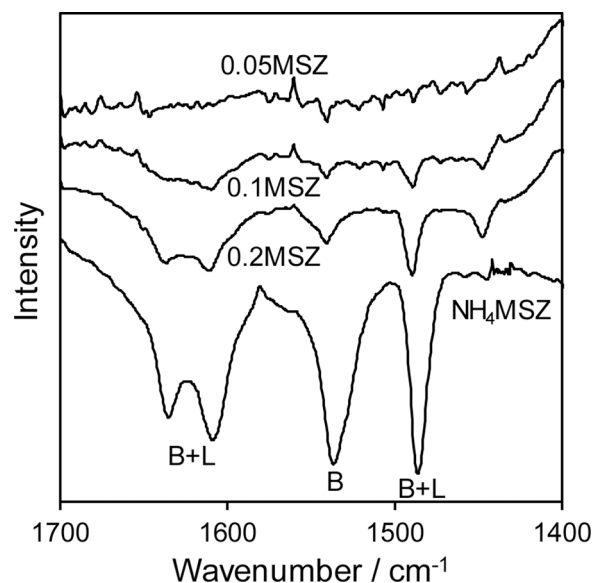


Fig. 3. DRIFT spectra of pyridine titrated, magnetic sulfated $\text{Fe}_3\text{O}_4@\text{SiO}_2@\text{ZrO}_2$ nanoparticles with Brønsted and Lewis acid bands indicated.

increased both the sulfate surface density (and hence acid loading) and the overall degree of sulfation of the zirconia shell (and hence significantly enhanced S 2p XP signal and surface S content). DRIFT spectra of the pyridine titrated, sulfated magnetic nanoparticles shown Fig. 3 all display similar strong (predominantly) Brønsted acid features, with a characteristic pure Brønsted band at 1535 cm^{-1} , and hence common acid character; any differences in their reactivity are therefore likely to reflect their differing acid loading (rather than Brønsted/Lewis acid character).

The performance of MSZ nanoparticles was subsequently evaluated for propanoic acid esterification with methanol under mild conditions. Fig. 4 shows the rate of esterification was directly proportional to acid site loading, with the H_2SO_4 impregnated MSZ nanoparticles exhibiting poor activity compared to a pure SZ reference, whereas the NH_4MSZ nanoparticles were approximately four times more active than SZ (165 versus $44\text{ mmol h}^{-1}\text{ g}^{-1}$) and achieved 93% conversion in only 1 h. Recycle data on the most active NH_4MSZ catalyst revealed a modest loss of activity loss between a first and second reaction (propanoic acid conversion after 6 h falling from $100 \rightarrow 71\%$) possibly due to leaching of weakly bound sulfate species or poisoning of strong acid sites by organic residues.

Corresponding Turnover Frequencies (TOFs) normalised per acid site reveal a monotonic increase from $5 \rightarrow 52\text{ h}^{-1}$ with $[\text{H}_2\text{SO}_4]$ for the H_2SO_4 impregnated MSZs (Fig. 5); this is attributed to a concomitant

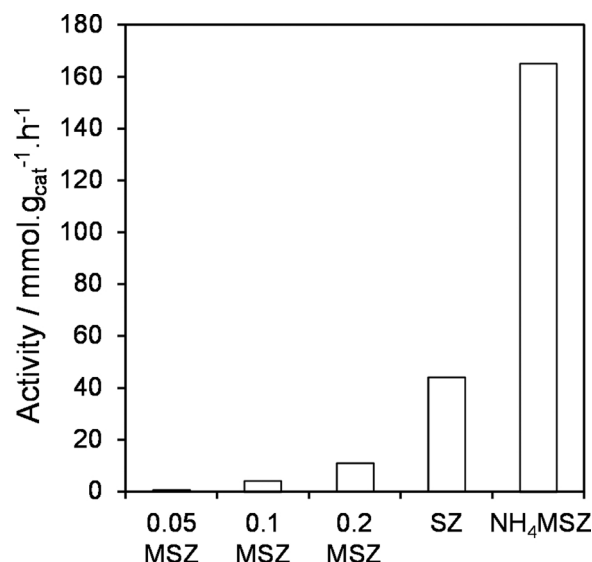


Fig. 4. Activity of conventional SZ and magnetic sulfated $\text{Fe}_3\text{O}_4@\text{SiO}_2@\text{ZrO}_2$ nanoparticles for propanoic acid esterification with methanol. Reaction conditions: 60°C , 12.5 mL MeOH, 50 mg catalyst, molar MeOH:propanoic acid (30:1).

Table 1

Surface and bulk properties of parent and sulphated magnetic $\text{Fe}_3\text{O}_4@\text{SiO}_2@\text{ZrO}_2$ nanoparticles.

Sample ^a	SO_4^{2-} precursor/ mmol	Surface area ^b / $\text{m}^2\text{ g}^{-1}$	Pore volume / $\text{cm}^3\text{ g}^{-1}$	BJH pore diameter ^c /nm	Surface S content ^d /at%	Bulk S content ^e /wt%	Acid site loading ^f / mmol g^{-1}
$\text{Fe}_3\text{O}_4@\text{SiO}_2@\text{ZrO}_2$	–	93	0.14	3.4	–	–	–
0.05MSZ	1.5	112	0.23	3.9	0.25	0.21	0.25
0.1MSZ	3	123	0.23	1.5	0.47	0.27	0.32
0.2MSZ	6	130	0.24	3.9	1.19	0.47	0.42
NH_4MSZ	2.3	42	0.19	1.5	4.19	7.29	2.75
SZ	–	172	0.24	3.4	–	3.23	0.78

^a MSZ and NH_4MSZ refers to $\text{Fe}_3\text{O}_4@\text{SiO}_2@\text{ZrO}_2$ nanoparticles sulphated using H_2SO_4 or $(\text{NH}_4)_2\text{SO}_4$ respectively, the prefix refers to the $[\text{H}_2\text{SO}_4]$ employed.

^b BET analysis.

^c from desorption branch of N_2 physisorption isotherm.

^d from XPS.

^e from CHNS elemental analysis.

^f from propylamine TGA-MS.

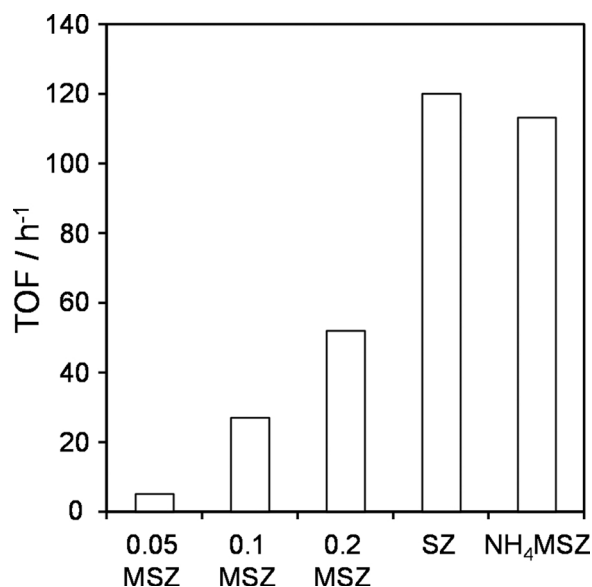


Fig. 5. TOFs of magnetic sulfated $\text{Fe}_3\text{O}_4@/\text{SiO}_2@/\text{ZrO}_2$ nanoparticles and conventional SZ for propanoic acid esterification with methanol. Reaction conditions: 60 °C, 12.5 mL MeOH, 50 mg catalyst, molar MeOH:propanoic acid (30:1).

increase in acid strength, as previously observed for both pure SZ and SZ conformal monolayers grown on mesoporous silica frameworks [22,42]. However, the NH_4MSZ TOF of 113 h^{-1} was comparable to that of pure SZ possessing strong acid sites, while offering the benefit of facile magnetic separation post-reaction. Since TOFs do not convey information regarding the number of active sites, which is critical to their potential industrial exploitation, due consideration must be given to the specific activity (mass normalised rates of propanoic esterification) when benchmarking against commercial catalysts. Fig. 4 highlights the clear superiority of our NH_4MSZ catalyst versus pure SZ in this regard.

4. Conclusions

A new method for the preparation of magnetically-separable $\text{Fe}_3\text{O}_4@/\text{SiO}_2@/\text{SO}_4\text{-ZrO}_2$ core-shell nanoparticle catalysts has been developed. The thickness of the ZrO_2 shell in parent $\text{Fe}_3\text{O}_4@/\text{SiO}_2@/\text{ZrO}_2$ nano-particles could be controlled by adjusting the zirconium butoxide to Lutensol AO5 ratio, with 1:10 is confirmed to be the optimal ratio to give rise to mono-dispersed ZrO_2 nano-spheres. Sulfation of $\text{Fe}_3\text{O}_4@/\text{SiO}_2@/\text{ZrO}_2$ nanoparticles using $(\text{NH}_4)_2\text{SO}_4$ is less corrosive towards the ZrO_2 shell, generating materials with higher acid sites loadings (2.75 mmol g^{-1}) than achievable with H_2SO_4 (0.42 mmol g^{-1}). All $\text{Fe}_3\text{O}_4@/\text{SiO}_2@/\text{SO}_4\text{-ZrO}_2$ samples were active for propanoic acid esterification, with the NH_4MSZ sample exhibiting a TOF of 113 h^{-1} , comparable to that of pure SZ but with the added advantage of magnetic separation. Future work will explore the use of mesoporous silica priming layers to further increase the surface area of the central $\text{Fe}_3\text{O}_4@/\text{SiO}_2$ nanoparticle [15] prior to ZrO_2 grafting [42].

Acknowledgements

We thank the EPSRC for financial support under EP/K014676/1 and the Royal Society for the award of an Industry Fellowship to KW.

Appendix A. Supplementary data

Supplementary data associated with this article can be found, in the

online version, at <http://dx.doi.org/10.1016/j.mcat.2018.02.021>.

References

- [1] V. Polshettiwar, R. Luque, A. Fihri, H. Zhu, M. Bouhrara, J.-M. Basset, *Chem. Rev.* 111 (2011) 3036–3075.
- [2] A.-H. Lu, E.L. Salabas, F. Schüth, *Angew. Chem. Int. Ed.* 46 (2007) 1222–1244.
- [3] R. Liu, Y. Guo, G. Odusote, F. Qu, R.D. Priestley, *ACS Appl. Mater. Interfaces* 5 (2013) 9167–9171.
- [4] H. Tan, J.M. Xue, B. Shuter, X. Li, J. Wang, *Adv. Funct. Mater.* 20 (2010) 722–731.
- [5] H.-Y. Lin, W.-Y. Chen, Y.-C. Chen, *Anal. Bioanal. Chem.* 394 (2009) 2129–2136.
- [6] J. Liu, S.Z. Qiao, S. Budi Hartono, G.Q. Lu, *Angew. Chem. Int. Ed.* 49 (2010) 4981–4985.
- [7] Y. Deng, D. Qi, C. Deng, X. Zhang, D. Zhao, *J. Am. Chem. Soc.* 130 (2007) 28–29.
- [8] T. Tago, T. Hatsuta, K. Miyajima, M. Kishida, S. Tashiro, K. Wakabayashi, *J. Am. Ceram. Soc.* 85 (2002) 2188.
- [9] J. Lee, Y. Lee, J.K. Youn, H.B. Na, T. Yu, H. Kim, S.M. Lee, Y.M. Koo, J.H. Kwak, H.G. Park, H.N. Chang, M. Hwang, J.G. Park, J. Kim, T. Hyeon, *Small* 4 (2008) 143–152.
- [10] P. Tartaj, T. González-Carreño, C.J. Serna, *Adv. Mater.* 13 (2001) 4.
- [11] D.-M. Lai, L. Deng, Q.-X. Guo, Y. Fu, *Energy Environ. Sci.* 4 (2011) 3552–3557.
- [12] X. Zhang, M. Wang, Y. Wang, C. Zhang, Z. Zhang, F. Wang, J. Xu, *Chin. J. Catal.* 35 (2014) 703–708.
- [13] S. Wang, Z. Zhang, B. Liu, J. Li, *Catal. Sci. Technol.* 3 (2013) 2104.
- [14] R. Fang, R. Luque, Y. Li, *Green Chem.* 18 (2016) 3152–3157.
- [15] Z. Tai, M.A. Isaacs, C.M.A. Parlett, A.F. Lee, K. Wilson, *Catal. Commun.* 92 (2017) 56–60.
- [16] H. Wang, J. Covarrubias, H. Prock, X. Wu, D. Wang, S.H. Bossmann, *J. Phys. Chem. C* 119 (2015) 26020–26028.
- [17] Zillillah, G. Tan, Z. Li, *Chemistry* 14 (2012) 3077–3086.
- [18] S. Shylesh, V. Schünemann, W.R. Thiel, *Angew. Chem. Int. Ed.* 49 (2010) 3428–3459.
- [19] N. Tokmoldin, N. Griffiths, D.D.C. Bradley, S.A. Haque, *Adv. Mater.* 21 (2009) 3475–3478.
- [20] M. Levichkova, V. Mankov, N. Starbov, D. Karashanova, B. Mednikarov, K. Starbova, *Surf. Coatings Technol.* 141 (2001) 7.
- [21] I.W. Chen, L.A. Xue, *J. Am. Ceram. Soc.* 73 (1990) 2585–2609.
- [22] A. Osatiashtiani, A.F. Lee, D.R. Brown, J.A. Melero, G. Morales, K. Wilson, *Catal. Sci. Technol.* 4 (2014) 333–342.
- [23] X.M. Song, A. Sayari, *Catal. Rev.-Sci. Eng.* 38 (1996) 329–412.
- [24] A. Osatiashtiani, L.J. Durndell, J.C. Manayil, A.F. Lee, K. Wilson, *Green Chem.* 18 (2016) 5529–5535.
- [25] M.A. Ecomier, K. Wilson, A.F. Lee, *J. Catal.* 215 (2003) 57–65.
- [26] H. Ghafari, A. Rashidzadeh, B. Ghorbani, M. Talebi, *New J. Chem.* 39 (2015) 4821–4829.
- [27] W. Wang, H. Zhang, L. Zhang, H. Wan, S. Zheng, Z. Xu, *Colloid Surface A* 469 (2015) 100–106.
- [28] H.-P. Peng, R.-P. Liang, L. Zhang, J.-D. Qiu, *Electrochim. Acta* 56 (2011) 4231–4236.
- [29] G.S. Chaubey, J. Kim, *Bull. Korean Chem. Soc.* 28 (2007) 4.
- [30] A. Sarkar, S.K. Biswas, P. Pramanik, *J. Mater. Chem.* 20 (2010) 8.
- [31] J. Yin, X. Qian, J. Yin, M. Shi, J. Zhang, G. Zhou, *Inorg. Chem. Commun.* 6 (2003) 942–945.
- [32] P.M. Arnal, C. Weidenthaler, F. Schüth, *Chem. Mater.* 18 (2006) 2733–2739.
- [33] J.C. Manayil, V.C. dos Santos, F.C. Jentoft, M. Granollers Mesa, A.F. Lee, K. Wilson, *ChemCatChem* 9 (2017) 2231–2238.
- [34] J.C. Manayil, A. Osatiashtiani, A. Mendoza, C.M.A. Parlett, M.A. Isaacs, L.J. Durndell, C. Michailof, E. Heracleous, A. Lappas, A.F. Lee, K. Wilson, *ChemSusChem* 10 (2017) 3506–3511.
- [35] A. Osatiashtiani, B. Puértolas, C.C.S. Oliveira, J.C. Manayil, B. Barbero, M. Isaacs, C. Michailof, E. Heracleous, J. Pérez-Ramírez, A.F. Lee, K. Wilson, *Biomass Convers. Biorefin.* 7 (2017) 331–342.
- [36] L. Ciddor, J.A. Bennett, J.A. Hunns, K. Wilson, A.F. Lee, *J. Chem. Technol. Biot.* 90 (2015) 780–795.
- [37] W.R. Zhao, J.L. Gu, L.X. Zhang, H.R. Chen, J.L. Shi, *J. Am. Chem. Soc.* 127 (2005) 8916–8917.
- [38] O. Kresnawahjuesa, R.J. Gorte, D.D. Oliveira, L.Y. Lau, *Catal. Lett.* 82 (2002) 6.
- [39] E. Matijević, P. Scheiner, *J. Colloid Interface Sci.* 63 (1978) 509–524.
- [40] A.I.M. Rabee, G.A.H. Mekhemer, A. Osatiashtiani, M.A. Isaacs, A.F. Lee, K. Wilson, M.I. Zaki, *Catalysts* 7 (2017).
- [41] M.A. Ecomier, A.F. Lee, K. Wilson, *Microporous Mesoporous Mater.* 80 (2005) 301–310.
- [42] A. Osatiashtiani, A.F. Lee, M. Granollers, D.R. Brown, L. Olivi, G. Morales, J.A. Melero, K. Wilson, *ACS Catal.* 5 (2015) 4345–4352.
- [43] W.H. Gries, *Surf. Interface Anal.* 24 (1996) 38–50.